

## Electronic Supplementary Information (ESI)

### **Dendrite-free Zn electrodeposition triggered by interatomic orbital hybridization of Zn and single vacancy carbon defect for aqueous Zn-based flow batteries**

Ju-Hyuk Lee,<sup>a</sup> Riyul Kim,<sup>ac</sup> Soohyun Kim,<sup>ac</sup> Jiyun Heo,<sup>ac</sup> Hyeokjin Kwon,<sup>a</sup> Jung Hoon Yang,<sup>b</sup> Hee-Tak Kim<sup>\*ac</sup>

<sup>a</sup> *Department of Chemical and Biomolecular Engineering, KAIST, 291 Daehak-ro, Yuseong-gu, Daejeon 34141, Republic of Korea*

<sup>b</sup> *Energy Storage Laboratory, Korea Institute of Energy Research, 152 Gajeong-ro, Yuseong-gu, Daejeon, 34129, Republic of Korea*

<sup>c</sup> *Advanced Battery Center, KAIST Institute for the NanoCentury, KAIST, 291, Daehak-ro, Yuseong-gu, Daejeon 34141, Republic of Korea*

\* Email: Hee-Tak Kim: [heetak.kim@kaist.ac.kr](mailto:heetak.kim@kaist.ac.kr)

## 1. Experimental section

### 1.1. Synthesis of electrodes

ZIF-8@CF: CF ( $3 \times 2 \text{ cm}^2$ ) was surface oxidized at  $520^\circ\text{C}$  for 9 h under an oxygen ( $\text{O}_2$ ) gas stream for hydrophilicity. After cooling to room temperature, the surface-oxidized CF was decorated with ZIF-8. Zinc nitrate hexahydrate (5.95 g, 1 eq.) and 2-methyl imidazole (13.136 g, 8 eq.) were separately dissolved in 100 mL of methanol. The solutions of Zinc nitrate hexahydrate (15 mL) and 2-methyl imidazole (15 mL) were mixed, and the CFs were immersed and stirred in the mixed solution for 12 h. The CFs were then taken out of the solution, and thoroughly washed with ethanol for many times to remove any remaining solvents. The ZIF-8 coating procedure was repeated nine times. The resulting ZIF-8@CF was dried under a vacuum at  $60^\circ\text{C}$ .

CZs: ZIF-8@CF was transferred to a vacuum oven and heated to the carbonization temperature ( $1000^\circ\text{C}$ ) at  $5^\circ\text{C min}^{-1}$  under a nitrogen ( $\text{N}_2$ ) atmosphere for 1 h and 5 h for the CZ-1 and CZ-5 electrodes, respectively. The resultant CZs were transferred to a beaker containing 2 M hydrochloric acid and stored with stirring for 6 h at room temperature. CZs were sequentially rinsed with distilled water many times and were evacuated for 6 h at  $70^\circ\text{C}$ .

### 1.2. Characterization

The X-ray diffraction was performed at 5.0 kV using a XRD system (model: D/MAX-2500) with an angle range from  $10^\circ$  to  $90^\circ$  and a scanning rate of  $5^\circ\text{C min}^{-1}$ . TEM and HAADF-STEM images coupled with EDS were obtained on an FEI Talos F200X TEM at an acceleration voltage of 300 kV. The surface morphology of the deposits was analyzed by SEM on an FE-SEM (Sirion, Netherlands). Raman spectra were obtained by using a WITec CRM200 confocal Raman microscopy system with a laser wavelength of 488 nm and a spot size of 0.5 mm. The surface analysis of the sample was carried out using a Thermo Scientific Theta Probe X-ray photoelectron spectroscope. The BET surface area measurements were carried out using a Micromeritics ASAP 2010 apparatus (Micromeritics Instrument Corporation, Norcross, GA, USA). Samples were degassed at  $200^\circ\text{C}$  for 12 h and degassed samples and sample tubes weighed before analysis.  $\text{N}_2$  adsorption analysis were carried out under liquid nitrogen (77 K) and surface areas calculated using the BET method by considering consistency criteria. Ultraviolet spectroscopy (UPS) and reflected electron energy loss spectroscopy (REELS) measurements were performed in a Thermo Scientific ESCALAB 250Xi spectrometer using a helium (He) discharge lamp optimized for He I line (21.2 eV) for UPS and a 1 KeV electron beam for REELS. Before UPS and REELS measurement, samples were cleaned by  $\text{Ar}^+$  sputtering treatment and their duration was 120 sec at an ion energy of 10 KeV with a 4 mm raster size. The values for Fermi level were determined by using gold metal as a reference. The HOMO value actually has a negative value. The Zn electrodeposited electrodes were prepared using three-electrode electrochemical cell in the same electrolyte as used for ZBB cycling test

with Ag/AgCl reference electrode and pCF counter electrode.

### 1.3. Electrochemical analysis

For accurately characterizing the electrochemical properties of the electrodes, a new type of electrochemical analysis cell was used.<sup>1</sup> Cyclic voltammetry (CV) and chronoamperometry (CA) were measured using an electrochemical measurement device (VSP) from BioLogic Science Instruments. The CVs were recorded in a stable potential window of 0-0.5 V at various scan rates (10-140 mV s<sup>-1</sup>) in the same electrolyte as used in the ZBB cycling test. The 0.01 M ZnBr<sub>2</sub> electrolyte was used for the CA experiment.

### 1.4. Battery performance test

Commercial carbon felt (SGL carbon group, Germany) with uncompressed thickness of 4 mm was used. The negative and positive area were both 6 cm<sup>2</sup>, and they were separated by a SF-600 separator (Asahi). An electrolyte mixture (20 mL) of 2 M ZnBr<sub>2</sub> + 0.5 M ZnCl<sub>2</sub> + 4 M NH<sub>4</sub>Cl + 0.02 M N-ethyl N-methyl pyrrolidinium bromide (MEP) in deionized water was used for the flow cell testing. The catholyte and anolyte flow rate were adjusted to 50 mL min<sup>-1</sup>.

### 1.5. DFT calculation

All density functional theory (DFT) calculations were performed with the program package DMol<sup>3</sup> in Materials Studio from Accelrys, Inc. Dmol<sup>3</sup> uses numerical orbitals as basis functions, each of which corresponds to atomic orbitals. These works utilize a double-numeric-plus-polarization (DNP) function and a global orbital cutoff of 4.0 Å. The size of the DNP basis set is comparable to Gaussian 6-31G(d), but the DNP is more accurate than the corresponding Gaussian basis set. DFT calculations were performed with a gradient-corrected (GGA) functional with the Perdew-Bueke-Ernzerhof (PBE) exchange correlation functional. Tolerances of energy, gradient, and displacement convergence were 0.00001 hartree, 0.002 hartree/Å, and 0.005 Å, respectively. To avoid the interaction caused by the periodicity, a vacuum layer of 20 Å along the z-direction was used for calculations. The slab models were all built on the basis of a monolayer graphite (001) surface in a 3 × 3 × 1 supercell and 3 × 3 × 1 k-point. Monkhorst-Pack grids were adopted to the Brillouin zone. The force tolerance of self-consistent-field (SCF) cycles was 1.0 × 10<sup>-6</sup>. The Grimme's DFT-D2 method was adopted to account for the van der Waals interactions (vdW), and this method was optimized for several DFT functionals. The adsorption energies of Zn on different carbon surfaces were calculated as follows:  $E_{ads} = E_{Zn + Carbon\ surface} + E_{Zn} - E_{Carbon\ surface}$  where  $E_{Zn + Carbon\ surface}$  and  $E_{Carbon\ surface}$  are the DFT total energies of different carbon surfaces with and without Zn atoms adsorbed, respectively, and  $E_{Zn}$  is the energy of Zn, which

is obtained from an isolated atom.

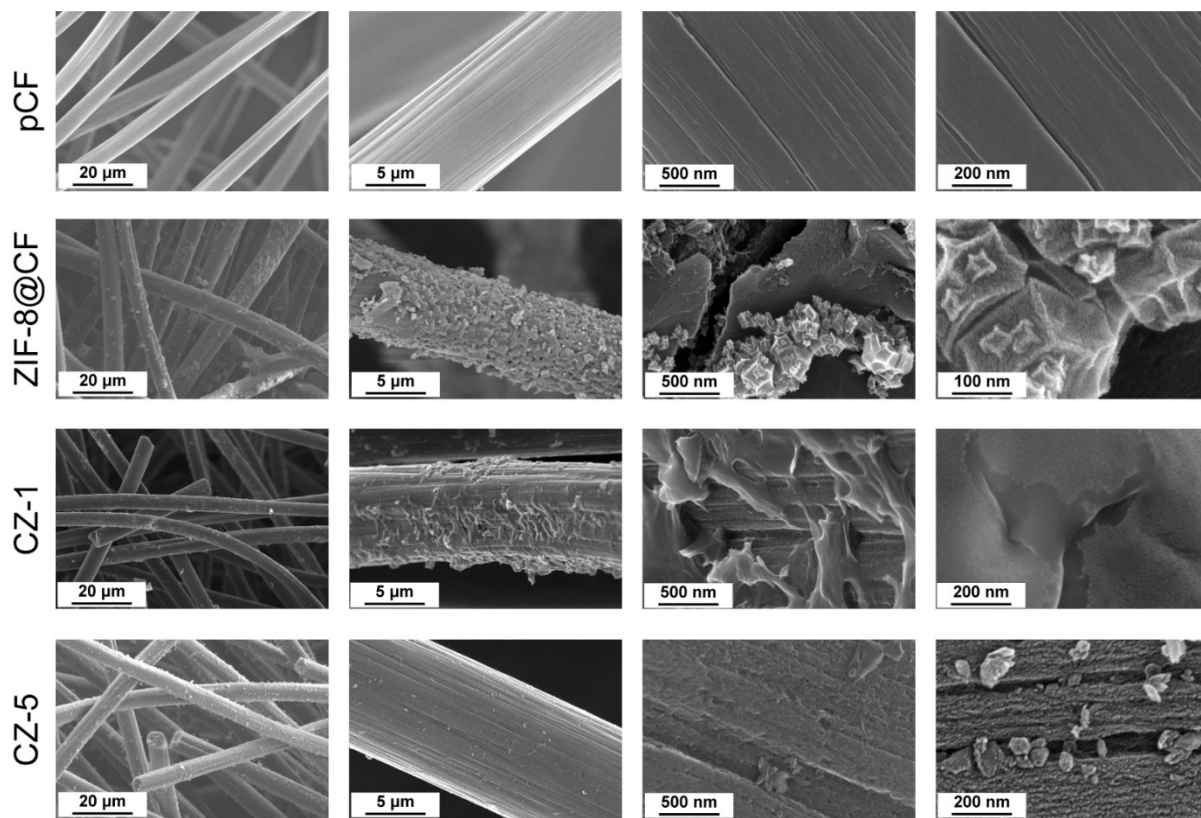


**Fig. S1** High-magnification SEM images of pCF, ZIF-8@CF, CZ-1 and CZ-5 electrode.

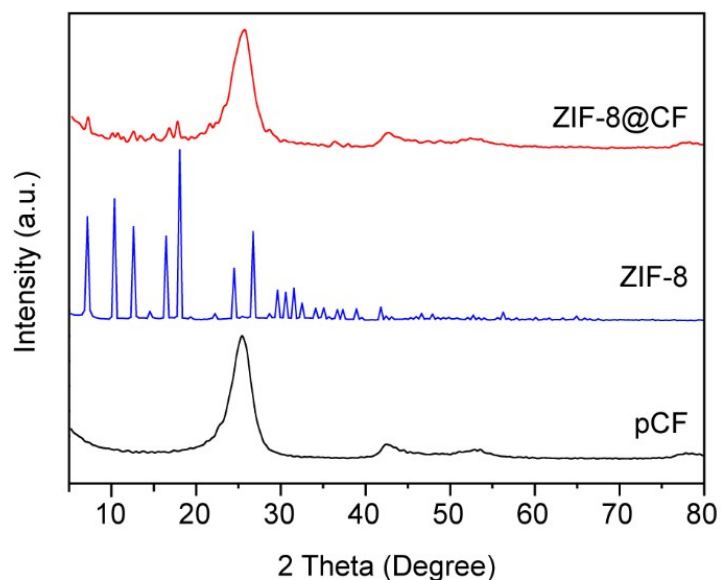


**Fig. S2** Powder X-ray diffraction (PXRD) patterns of pCF, ZIF-8 powder and ZIF-8-coated CF (ZIF-8@CF).

The PXRD pattern of the ZIF-8@CF electrode showed the characteristic peaks from ZIF-8 at 7.2, 10.2, 12.5, 16.0 and 17.7°, which corresponding to the (110), (200), (211), (310), and (222) plane, respectively. The result verified the successful growth of ZIF-8 crystal on the pCF electrode.

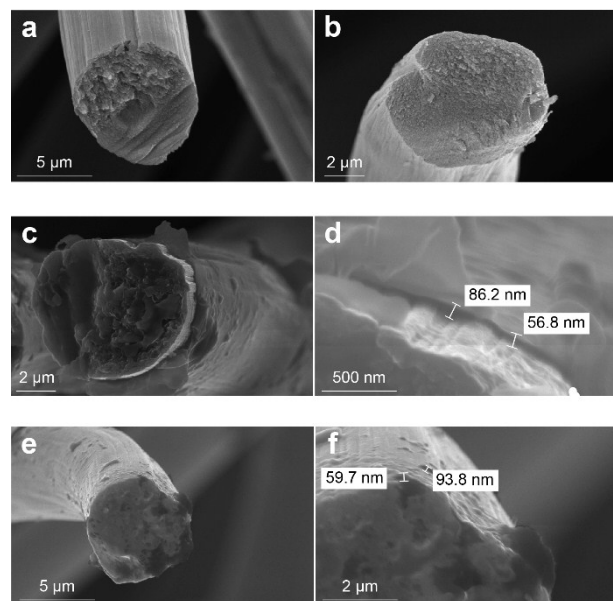


**Fig. S3** High magnification SEM images of (a,b) pCF, (c,d) CZ-1, and (e,f) CZ-5.

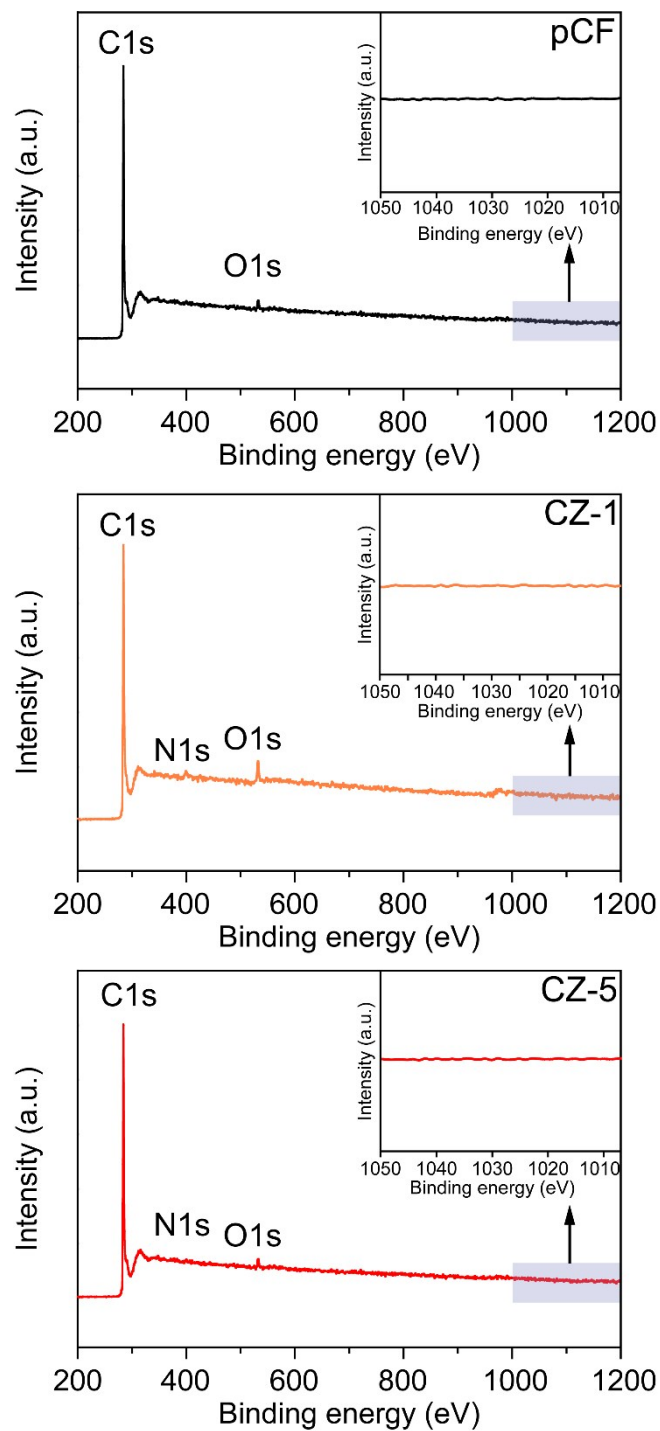


**Fig. S4** Representative element XPS surveys for pCF, CZ-1, and CZ-5 electrode (insets: magnified region corresponding to Zn 2p spectra)

**Table S1.** Elemental compositions of pCF, CZ-1 and CZ-5 determined from the XPS survey spectra.

Sample	Concentration (at.%)		
	C	O	N
pCF	97.83	2.17	-
CZ-1	93.62	3.97	2.41
CZ-5	94.48	4.1	1.21

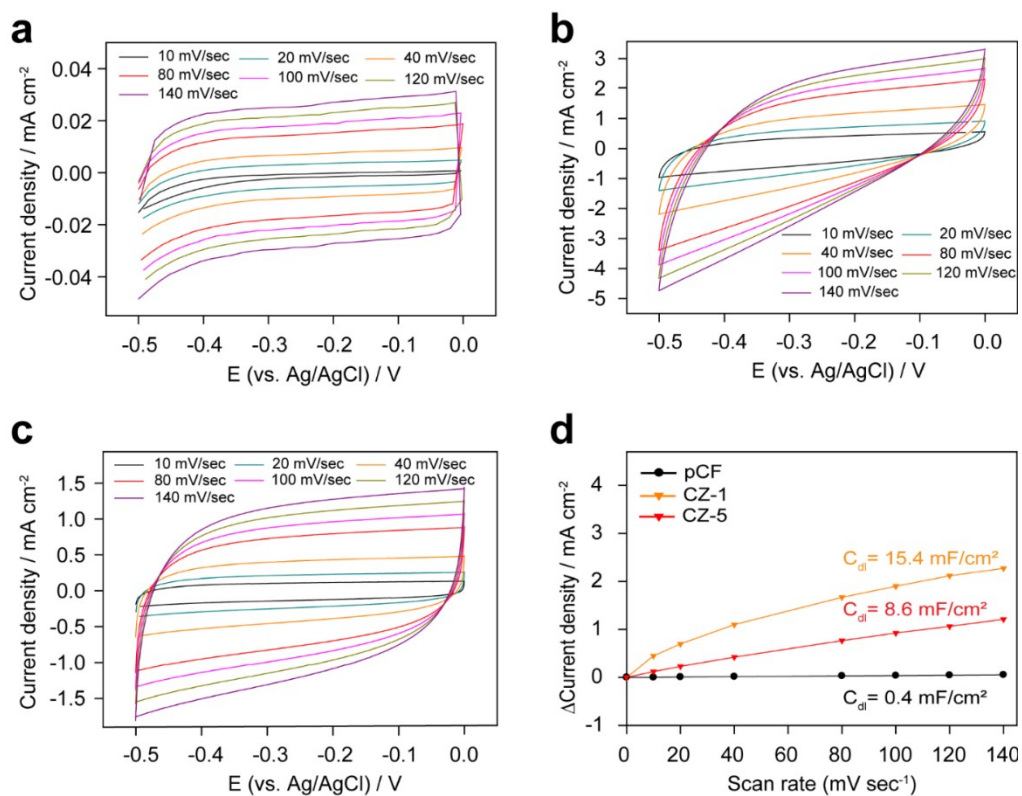


**Fig. S5** Cyclic voltammetry for (a) pCF, (b) CZ-1 and (c) CZ-5 electrode in the potential range of 0 to -0.5 V at various scan rates. (d) Plot of capacitive current as a function of scan rate for pCF, CZ-1 and CZ-5 electrode. Double layer capacitances were calculated from the slopes in the plot (Capacitance = current/voltage sweep rate).

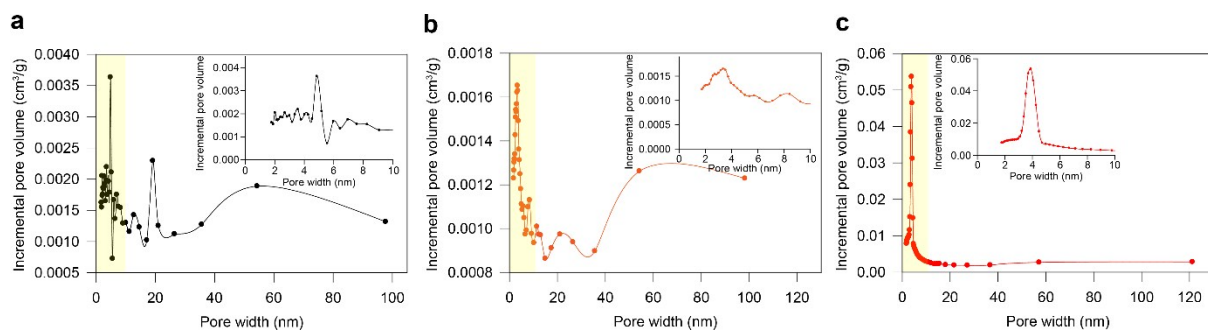


**Fig. S6** Pore size distributions obtained from N<sub>2</sub> adsorption isotherms for (a) pCF, (b) CZ-1, and (c) CZ-5.

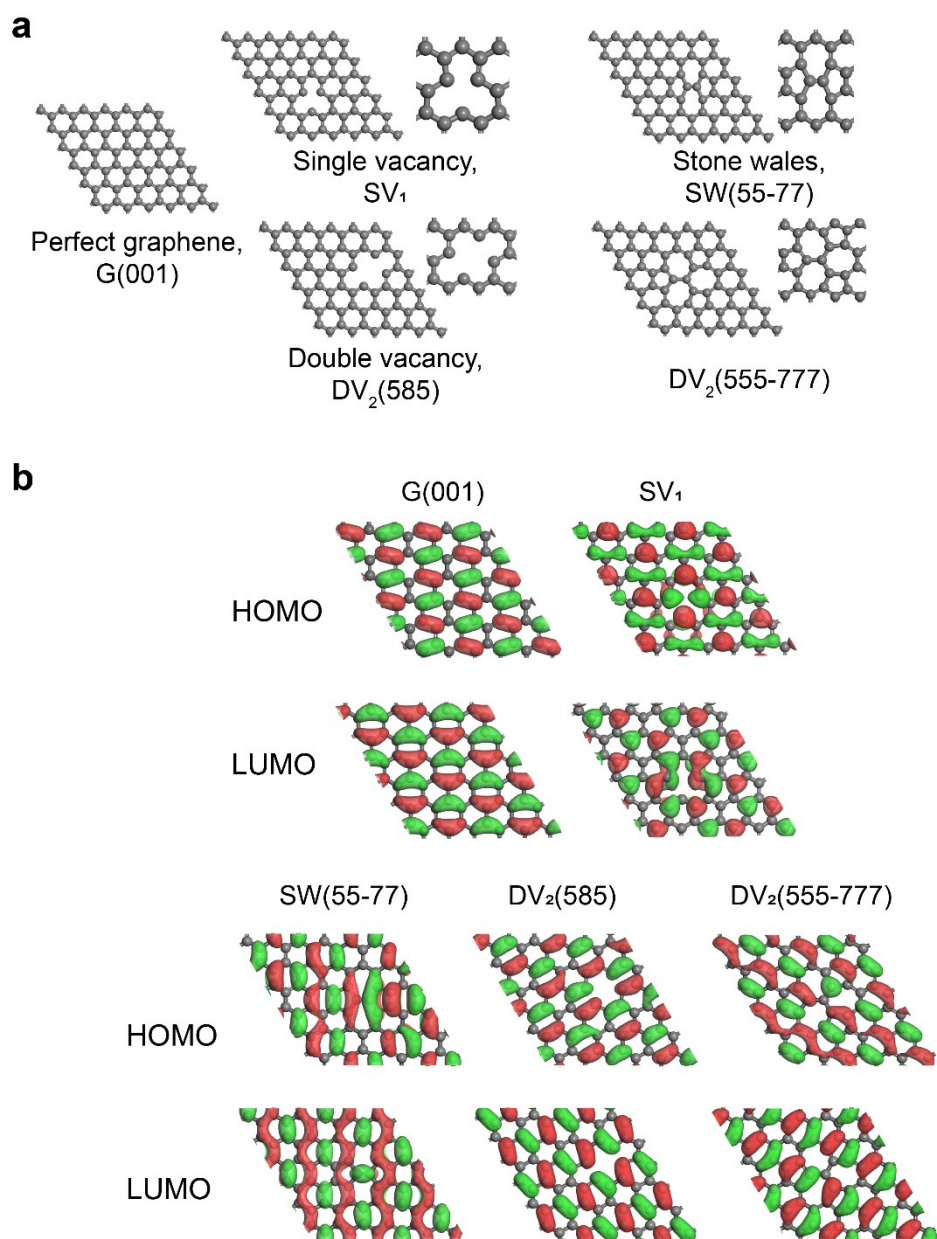


**Fig. S7** (a) Perfect graphene and defect structures and (b) HOMO/LUMO states for the perfect graphene and four carbon defects. The electron densities of HOMO and LUMO states are plotted for iso-values of 0.012 au with the red and green colors denoting the opposite signs.

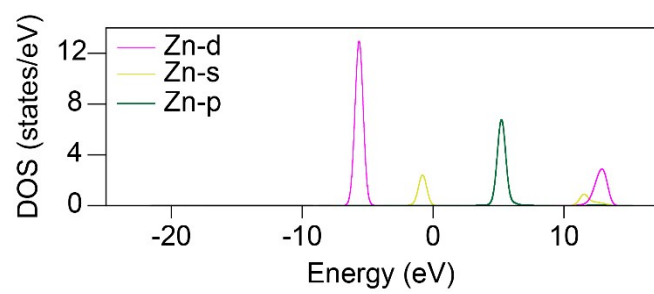


**Fig. S8** pDOS of isolated Zn.

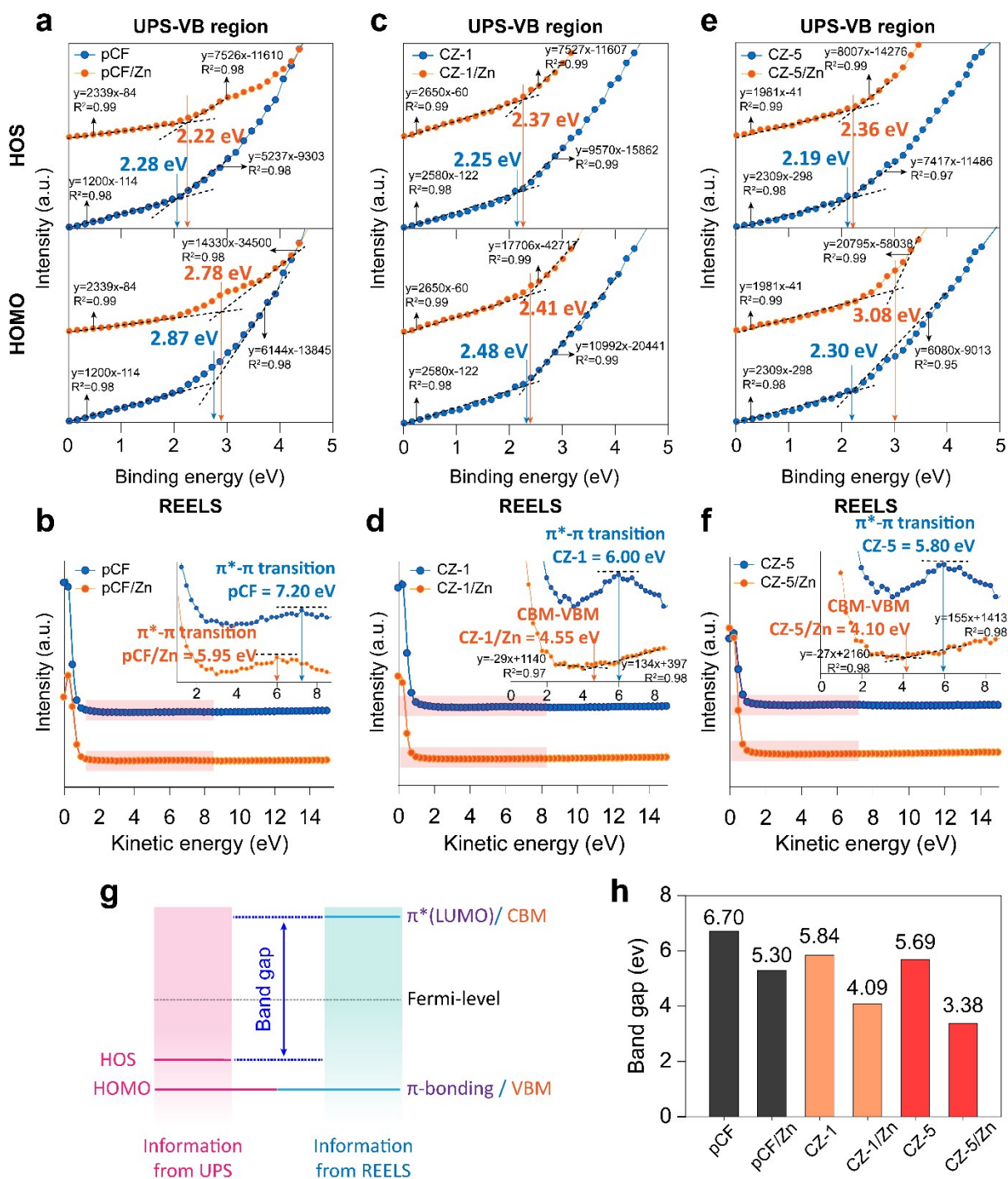


**Fig. S9** UPS valence band (VB) regions (a, c, e) and REELS spectra (b, d, f) for (a, b) pCF, (c, d) CZ-1, and (e, f) CZ-5 electrodes before and after a Zn deposition at  $100 \text{ mA cm}^{-2}$  for 60 s (Zn deposited electrodes are denoted as Zn/pCF, Zn/CZ-1, and Zn/CZ-5) (g) Schematic of energy levels for the band gap calculation. (h) Calculated band gaps for the electrodes before and after the Zn electrodeposition.

Fig. S9(a-f) showed UPS and REELS spectra for pCF, CZ-1, and CZ-5 electrodes before and after a Zn electrodeposition at  $100 \text{ mA cm}^{-2}$  for 60 s. In the UPS spectra, the distinguishable

bands closet to Fermi level are ascribed to highest occupied state (HOS) and highest occupied molecular orbital (HOMO). HOS and HOMO were quantified as indicated in the Fig. S9 a, c, and e. REELS revealed energy emission informing the difference between  $\pi$  (HOMO) and  $\pi^*$  (lowest occupied molecular orbital; LUMO) or between conduction band minimum (CBM) and valence band maximum (VBM).

Therefore, by combining UPS and REELS data, we determined the values for band gap (difference between HOS and LUMO) as schematically depicted in Fig. S9(g). The resulting band-gaps before and after Zn deposition were compared for pCF, CZ-1, and CZ-5 in Fig. S9(h). For all the electrodes, Zn deposition leads to a decrease of band gap, indicating the orbital hybridization at their defects. Remarkably, the band gap change was much larger for CZ-5 electrode, as expected from the band gap narrowing due to strong orbital hybridization with  $s p$  orbital of carbon in  $SV_1$  with Zn  $s p d$  orbitals in DFT calculations. The band gap analysis provides experimental evidence for the orbital hybridization.

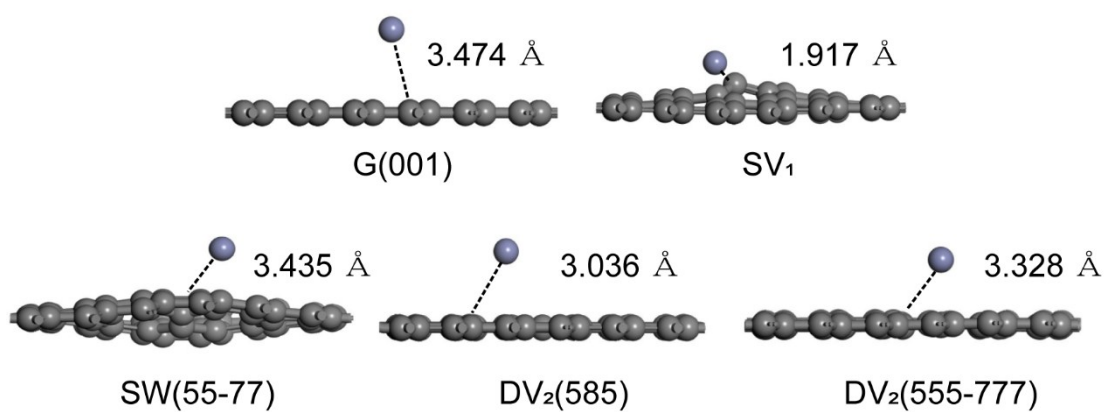


**Fig. S10** Optimized atomic structures of G(001), SV<sub>1</sub>, SW(55-77), DV<sub>2</sub>(585), and DV<sub>2</sub>(555-777) with Zn adatom.

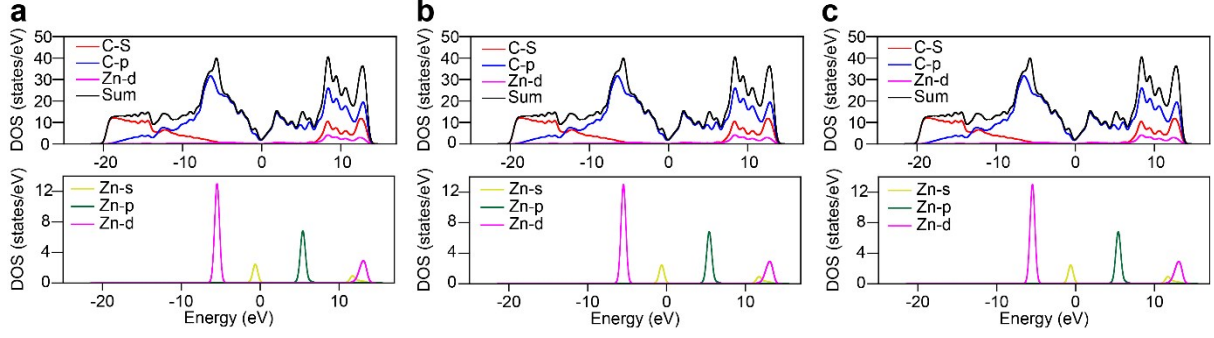


**Fig. S11** Total DOS and pDOS for (a) SW(55-77), (b) DV<sub>2</sub>(585), and (c) DV<sub>2</sub>(555-777) after Zn adsorption. The fermi energy is set at zero.

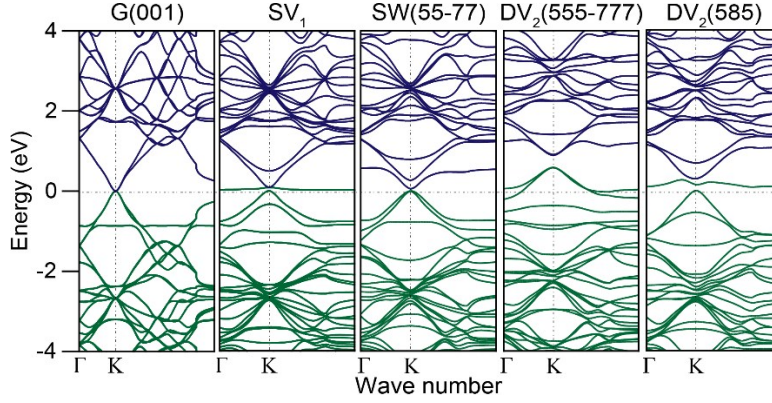


**Fig. S12** Band structures for G(001), SV<sub>1</sub>, SW(55-77), DV<sub>2</sub>(585) and DV<sub>2</sub>(555-777) after Zn adsorption. The fermi energy is set at zero.

**Table S2. Fermi-level of the various carbon surfaces determined from DFT calculation.**

	G(001)	SV <sub>1</sub>	SW(55-77)	DV <sub>2</sub> (555-777)	DV <sub>2</sub> (585)
Before Zn adsorption	-4.604	-4.656	-4.671	-5.088	-4.642
After Zn adsorption	-4.621	-4.498	-4.681	-5.044	-4.552

To obtain electronic band structures, we performed convergent calculation using 240 k-sampling point in the irreducible Brillouin zone (IBZ). Owing to the supercell used in the calculation, the K point of the  $1 \times 1$  graphene BZ is folded into the  $\Gamma$  point of the supercell BZ. Similarly, the M point of the  $1 \times 1$  graphene BZ is folded into the  $\Gamma$  of the supercell BZ (Fig S13). We calculated supercell BZ with M- $\Gamma$ -K-M line to follow the dispersion of the Dirac point. Correspondingly, the change of electronic structure with Zn adsorption for the representative carbon surfaces was traced (Fig. S12 and Table S2). Before Zn adsorption, the comparison of Fermi-level among G(001) and various carbon defects shows that Fermi-level is lowered with introducing the defects. It can be understood as such that the electron-deficiency due to the loss of carbon atom shifts Fermi-level down to valence band like p-type

doping in semiconductor. The adsorption of Zn adatom leads to an increase of Fermi-level for  $SV_1$ ,  $DV_2(555-777)$  and  $DV_2(585)$ , because Zn adatoms provide electrons to the electron-deficient carbons. However,  $G(001)$  and  $SW(55-77)$  show a decreased Fermi-level with Zn adsorption because they do not have any removed or added atoms.

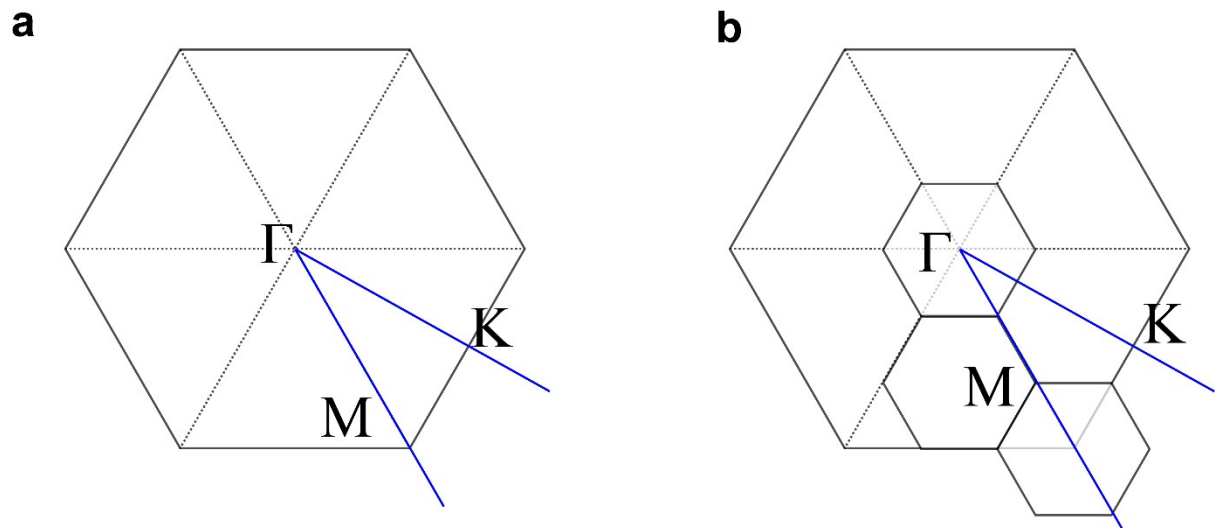


**Fig. S13** Brillouin zone (BZ) of (a)  $1 \times 1$  graphene and (b)  $3 \times 3$  graphene.

Owing to the supercell used in this study, the K point of the  $1 \times 1$  graphene BZ is folded into the  $\Gamma$  point of the supercell BZ.

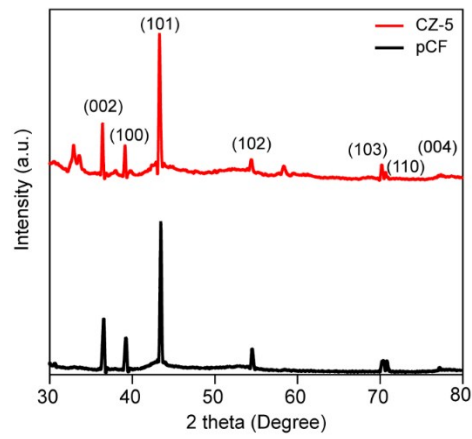


**Fig. S14** XRD patterns of the electrodeposited Zn on the pCF and CZ-5 electrode after imposing  $100 \text{ mA cm}^{-2}$  for 1.2 min.

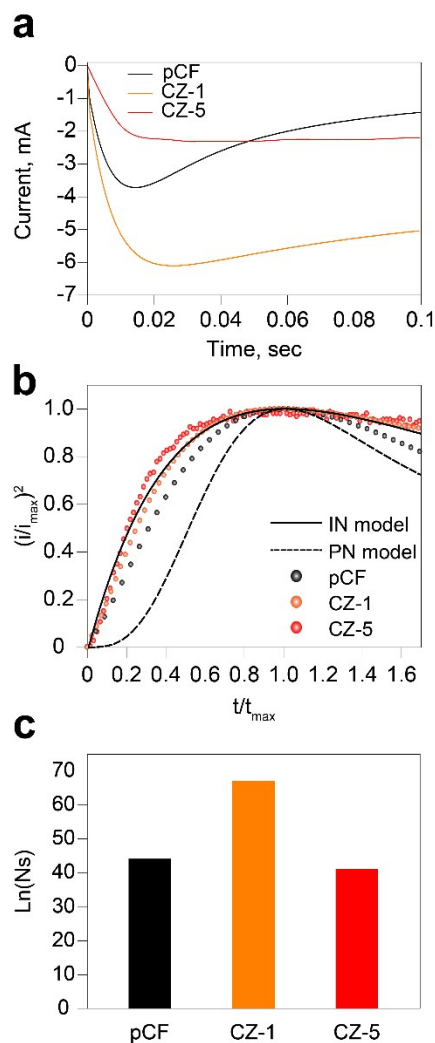


**Fig. S15** (a) Current-time responses of chronoamperometry at -1.46 V vs. Ag/AgCl for pCF, CZ-1, and CZ-5 electrode in contact with 0.01 M ZnBr<sub>2</sub> electrolyte. (b) Dimensionless plots of the current-time responses for pCF, CZ-1 and CZ-5 and theoretical responses from the S-H model. (c) Calculated densities of Zn nuclei for pCF, CZ-1 and CZ-5.

The nucleation behavior of electrodeposited Zn can be interpreted by using dimensionless mathematical model proposed by Scharifker-Hills (S-H).<sup>2</sup> The two types of dimensionless nucleation model (S-H model) are given in the following.

Instantaneous nucleation model (IN model):

$$\left(\frac{i}{i_m}\right)^2 = \frac{1.9542}{t/t_m} \left\{ 1 - \exp \left[ -1.2564 \left( \frac{t}{t_m} \right) \right] \right\}^2 \quad (1)$$

Progressive nucleation model (PN model):

$$\left(\frac{i}{i_m}\right)^2 = \frac{1.2254}{t/t_m} \left\{1 - \exp\left[-2.3367\left(\frac{t}{t_m}\right)\right]\right\}^2 \quad (2)$$

where  $i_m$  is the peak current,  $t_m$  is the corresponding time of peak current.

The experimental results well fit with the IN model. Therefore, the number density of formed nuclei ( $N_s$ ) can be calculated based on the IN model using the following equations.

$$i_m = 0.6382zFDc(kN)^{1/2} \quad (3)$$

$$k = (8\pi cM/\rho)^{1/2} \quad (4)$$

$$N_s = 1.2564/t_m \pi k D \quad (5)$$

$$i_m^2 t_m = 0.1629(zFc)^2 D \quad (6)$$

where  $D$  is the diffusion coefficient,  $c$  is the bulk concentration of the electroactive species,  $zF$  is the molar charge of the electrodepositing species,  $M$  and  $\rho$  are, respectively, the atomic weight and the density of the deposited materials.  $A$  is the steady-state nucleation rate constant per site,  $N_s$  is the number density of formed nuclei.

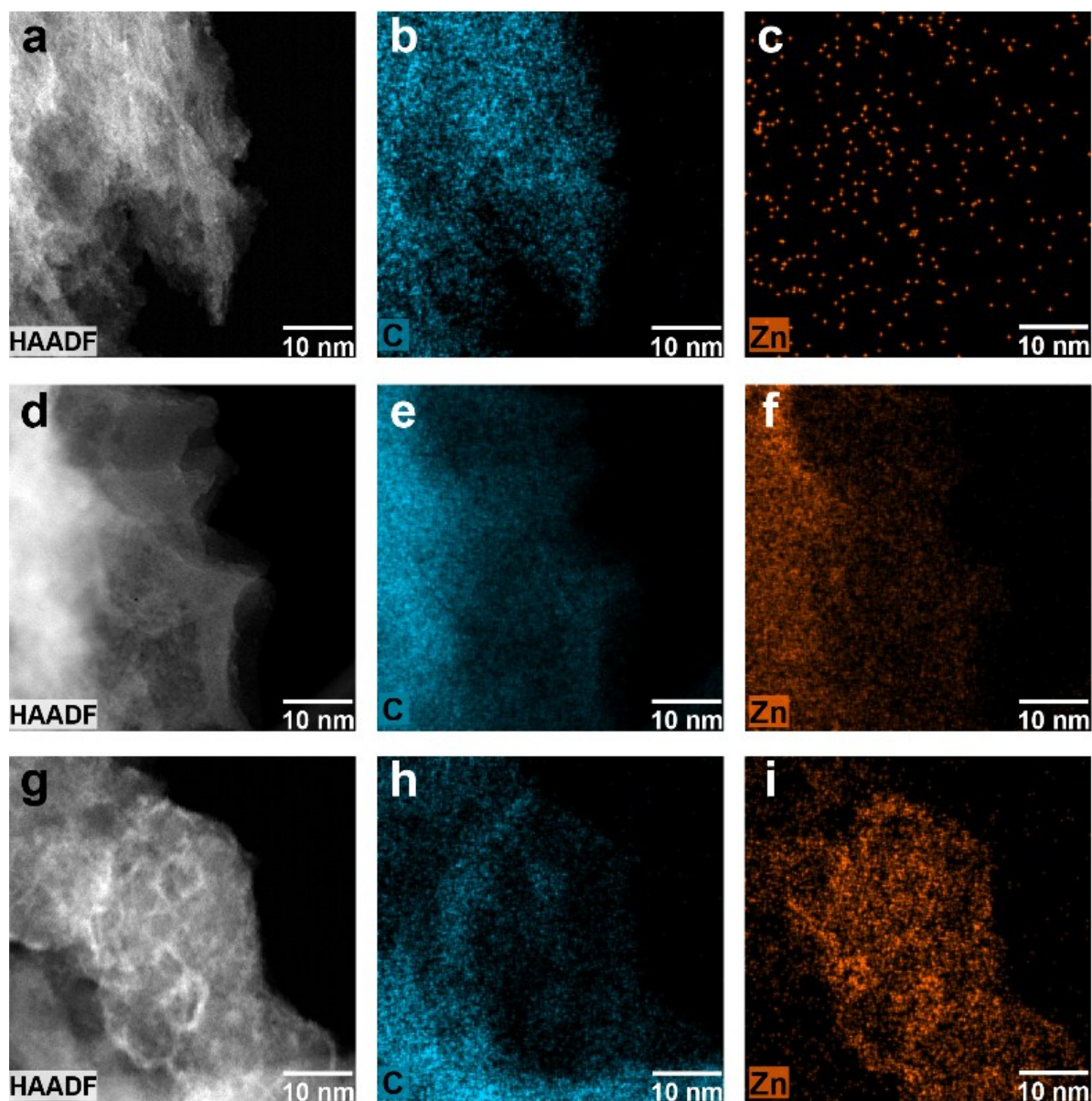


**Fig. S16** HAADF-STEM and EDS mapping images (C, Zn) for pCF, CZ-1 and CZ-5 after the electrodeposition of Zn at  $100 \text{ mA cm}^{-2}$  for 30 s. (a-c): pCF, (d-f): CZ-1, and (g-i) CZ-5.

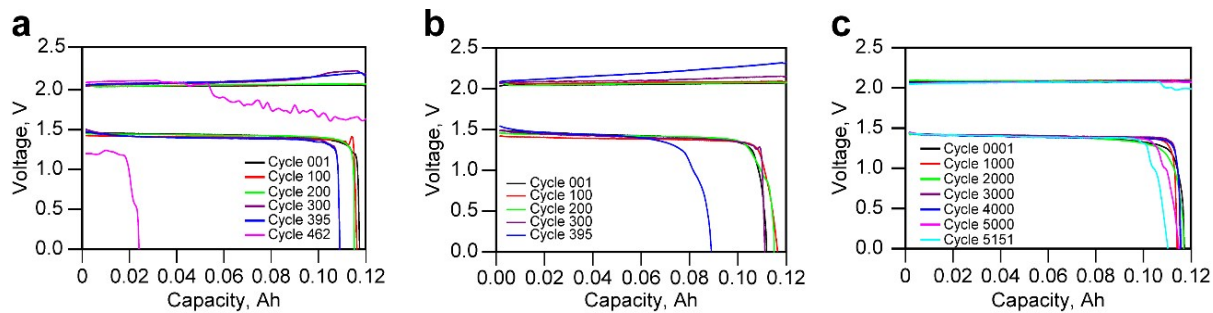


**Fig. S17** Charge-discharge voltage profiles for (a) pCF@ZBB, (b) CZ-1@ZBB and (c) CZ-5@ZBB at different cycle number during the long-term cycling test at  $100 \text{ mA cm}^{-2}$ .

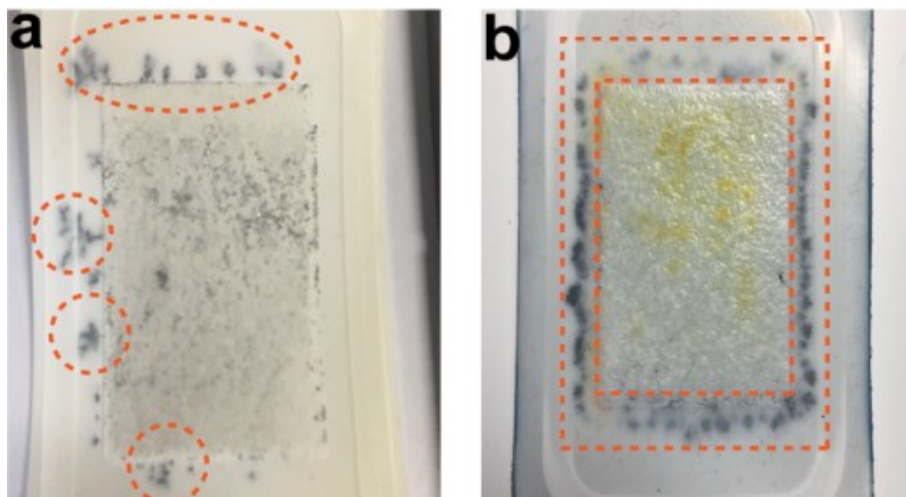


**Fig. S18** SEM images of the SF600 separators taken from (a) pCF@ZBB and (b) CZ-1@ZBB after the cycling test at  $100 \text{ mA cm}^{-2}$ .

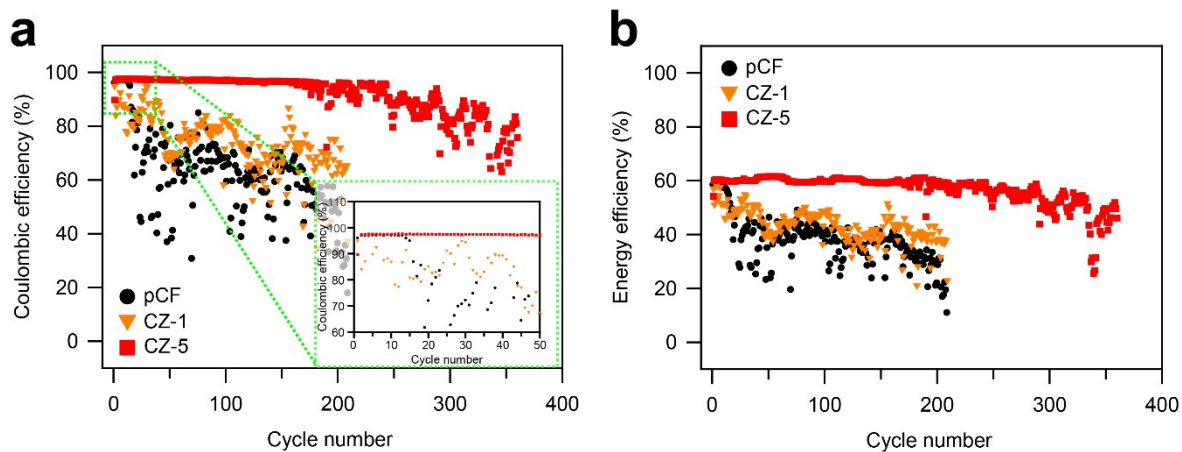


**Fig. S19** Galvanostatic cycling stability for ZBBs at  $120 \text{ mA cm}^{-2}$  and at  $20 \text{ mAh cm}^{-2}$ : (a) Coulombic efficiencies and (b) Energy efficiencies for the ZBBs with pCF, CZ-1 And CZ-5.

**Table S3.** Charging capacity, current density for charge/discharge, and number of cycle life of the previously reported various flow batteries and this work.

	Reference	Current density (mA cm <sup>-2</sup> )	Number of cycle life	Charging capacity (mAh)
Zn-Br	<b>This work</b>	100	5151	120
	[3]	20	350	120
	[4]	40	50	80
	[5]	80	100	100
	[6]	40	50	160
	[7]	80	100	160
	[8]	80	200	100
	[9]	40	45	298
	[10]	80	100	100
	[11]	160	100	360
	[12]	20	100	50
	[13]	20	100	90
	Zn-I	[14]	40	45
[15]		10	50	800
Zn-Fe	[16]	160	150	960
	[17]	20	45	25
Zn-Ce	[18]	30	50	180
	[19]	25	166	56.25

## Reference

1. J. H. Park, J. J. Park, O. O. Park, C.-S. Jin and J. H. Yang, *J. Power Sources*, 2016, **310**, 137-144.
2. G. Gunawardena, G. Hills, I. Montenegro and B. Scharifker, *J. Electroanal. Chem.*, 1982, **138**, 225-239.
3. R. Kim, S. Yuk, J.-H. Lee, C. Choi, S. Kim, J. Heo and H.-T. Kim, *J. Membr. Sci.*, 2018, **564**, 852-858.
4. M. Wu, T. Zhao, R. Zhang, H. Jiang and L. Wei, *Energy Technol.*, 2018, **6**, 333-339.
5. M. Wu, T. Zhao, R. Zhang, L. Wei and H. Jiang, *Electrochim. Acta*, 2018, **284**, 569-576.
6. H. Lin, L. Bai, X. Han, Y. Zhang and J. Shi, *Int. J. Electrochem. Sci.*, 2018, **13**, 12049-12061.
7. M. Wu, R. Zhang, K. Liu, J. Sun, K. Chan and T. Zhao, *J. Power Sources*, 2019, **442**, 227255
8. H. X. Xiang, A. D. Tan, J. H. Piao, Z. Y. Fu and Z. X. Liang, *Small*, 2019, **15**, 1901848.
9. S. Bae, J. Lee and D. S. Kim, *J Power Sources*, 2019, **413**, 167-173.
10. M. Wu, H. Jiang, R. Zhang, L. Wei, K. Y. Chan and T. Zhao, *Electrochim. Acta*, 2019, **318**, 69-75.
11. C. Wang, W. Lu, Q. Lai, P. Xu, H. Zhang and X. Li, *Adv. Mater.*, 2019, 1904690.
12. N. Venkatesan, K. S. Archana, S. Suresh, R. Aswathy, M. Ulaganathan, P. Periasamy and P. Ragupathy, *ChemElectroChem*, 2019, **6**, 1107-1114.
13. S. Suresh, M. Ulaganathan and R. Pitchai, *J. Power Sources*, 2019, **438**, 226998.
14. J. Liu, T. Ma, M. Zhou, S. Liu, J. Xiao, Z. Tao and J. Chen, *Inorg. Chem. Front.*, 2019, **6**, 731-735.
15. G.-M. Weng, Z. Li, G. Cong, Y. Zhou and Y.-C. Lu, *Energy Environ. Sci.*, 2017, **735**, 741.
16. Z. Yuan, Y. Duan, T. Liu, H. Zhang and X. Li, *iScience*, 2018, **3**, 40-49.
17. Y. Zhang, D. Henkensmeier, S. Kim, R. Hempelmann and R. Chen, *J. Energy Storage*, 2019, **25**, 100883.
18. Z. Xie, B. Liu, C. Xie, B. Yang, Y. Jiao, D. Cai, L. Yang, Q. Shu and A. Shi, *Mater. Chem. Phys.*, 2018, **220**, 208-215.
19. K. Amini and M. D. Pritzker, *Appl. Energy*, 2019, **255**, 113894.